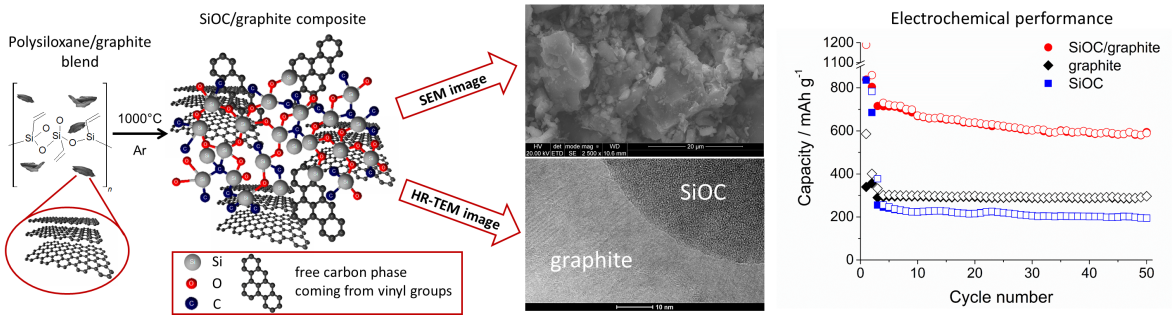

Postprint of: Knozowski D., Graczyk-Zając M., Vrankovic D., Trykowski G., Sawczak M., De Carolis D. M., Wilamowska-Zawłocka M., New insights on lithium storage in silicon oxycarbide/carbon composites: Impact of microstructure on electrochemical properties, COMPOSITES PART B-ENGINEERING, Vol. 225 (2021), 109302, DOI: 10.1016/j.compositesb.2021.109302

New insights on lithium storage in silicon oxycarbide/carbon composites: impact of microstructure on electrochemical properties

Dominik Knozowski [a], Magdalena Graczyk-Zając [b,c,*], Dragoljub Vrankovic [b, 1], Grzegorz Trykowski [d], Mirosław Sawczak [e], Dario M. De Carolis [b], Monika Wilamowska-Zawłocka [a,*]

[a] Department of Energy Conversion and Storage, Faculty of Chemistry, Gdańsk University of Technology, Narutowicza 11/12, 80-233 Gdańsk, Poland.

[b] Fachbereich Material und Geowissenschaften, Technische Universität Darmstadt, Otto-Berndt-Straße 3, 64287 Darmstadt, Germany.

[c] EnBW Energie Baden-Württemberg AG, Durlacher Allee 93, 76131 Karlsruhe, Germany

[d] Faculty of Chemistry, Nicolaus Copernicus University in Torun, 87-100 Toruń, Poland.

[e] Institute of Fluid Flow Machinery, Polish Academy of Sciences, Fiszera 14, 80-231 Gdańsk, Poland

***corresponding author: graczyk@materials.tu-darmstadt.de, m.graczyk-zajac@enbw.com, Tel: +49 1516 7162319, Fax: +49 721 63-17888**

monika.wilamowska@pg.edu.pl Tel: +48 58 347 24 74, Fax: +48 58 347 24 58

[1] present address: Mercedes-Benz AG, Mercedesstraße 120, 70327 Stuttgart, Germany

Abstract

In this work, we study the impact of the preceramic precursor vinyltriethoxysilane (VTES) on the electrochemical performance of silicon oxycarbide (SiOC) glass/graphite composites. We apply an innovative approach based on high-power ultrasounds in order to obtain highly homogenous composites with a uniform distribution of small graphitic flakes. This procedure enhances gelation and drying of VTES-based preceramic polymer/graphite blends. The SiOC/graphite composites reveal stable capacities (up to 520 mAh g^{-1} after 270 cycles), which are much higher than the sum derived from the ratio of the components. Additionally, the first cycle Coulombic efficiencies obtained for the composites are 15% higher than that of the pristine VTES-based SiOC ceramic. These properties are identified as the synergistic effect, originated from the addition of graphite to VTES-based SiOCs. Interestingly, such improvement in electrochemical performance is not noticed in the case of analogous SiOC/graphite composites based on phenyltriethoxysilane (PhTES) precursor. The microstructural investigation of the composites based on two different preceramic precursors using solid-state ^{29}Si NMR and Raman Spectroscopy unveils the reason for such discrepancy in their electrochemical behaviour.

Keywords: Polymer Derived Ceramics; Composites; Graphite; Li-ion Battery, Sol-Gel Synthesis

1. Introduction

Lithium-ion batteries are one of the most widespread devices for energy storage. However, relatively low power output and a very restricted temperature window limit their applications in emerging electric vehicles (EV) and hybrid electric vehicles (HEV)

[1,2]. One of the biggest challenges, in the creation of high power batteries, is to design electrode materials with excellent stability, high capacity and good capability upon the rapid charge-discharge current [3].

Graphitic anodes, used in commercial Li-ion batteries, provide stability and safety, but the capacity is limited to the theoretical value of 372 mAh g^{-1}. Thus, to meet the consumers' requirements for lighter, higher capacity and faster charge/discharge systems, there is a strong interest in developing new electrode materials. Polymer-derived silicon oxycarbides (SiOC) are considered as promising materials because of their high capacity, up to 600 mAh g^{-1}, excellent capability upon high charge-discharge current, low price and good availability of preceramic precursors [4–7]. The electrochemical properties of silicon oxycarbide (SiOC) ceramics with respect to reversible storage of lithium ions have been studied in the middle of the 1990s for the first time [4,8]. SiOC materials are typically prepared by the thermal conversion of polyorganosiloxanes under an inert atmosphere, by a so-called polymer-derived ceramic (PDC) process [9]. Preceramic polymers may be obtained, for instance, by the sol-gel method [10]. The microstructure of SiOC ceramics is typically composed of an amorphous Si-O-C network, interpenetrated by an amorphous free carbon phase. The amorphous Si-O-C network is built of tetrahedrally coordinated $SiO_{4-x}C_x$ (x = 1-4) structural units, including SiO_2 and C-enriched regions [11,12].

Though SiOC electrodes enable high capacities, they suffer from very high initial irreversible capacity, reaching even 60%, which severely limits their commercial applications. In our previous reports, [6,13] we demonstrated that the free carbon content plays a significant role in improving capacity, cyclic stability and limiting irreversible capacity; however the first cycle efficiency of synthesised ceramics did not exceed 63%.

Combining SiOC with carbonaceous materials is a common strategy to improve electrochemical performance, including first cycle efficiency [12,14–24]. For instance, Konno *et al.* [14] created SiOC-exfoliated graphite composites to minimize the amount of oxygen in the SiOC matrix. This led to Coulombic efficiency of the first cycle equal to ~70%, but the overall capability of the material faded after several tens of cycles. Kuksenko [17] produced SiOC ceramic with a high amount of disordered carbon achieving the first cycle Coulombic efficiency of about 80%, but this result was reported only for thin film (0.3 μm); for thicker electrodes, the efficiency was still equal to approx. 50%. Tahir *et al.* [18] performed prelithiation of SiOC by spray coating of stabilized lithium metal powder (SLMP®), resulting in an increase of first cycle efficiency from 48 to 86%. However, the prelithiation process is not applicable to all the binders and requires an inert atmosphere. Up to date, the best improvements of the first cycle efficiency were reported for SiOC composites with graphene, carbon nanotubes or carbon nanofibers [16,19–21,23,24]. Bhandavat *et al.* [19] created shell/core SiOC/carbon nanotube composites with the idea of decreasing amount of oxygen and creating paths for lithium diffusion. Such solution improved the first cycle efficiency from 50.1% achieved for pure SiOC to 67% recorded for the SiOC/CNTs shell/core composite. Sang *et al.* [20] produced SiOC/3D graphene scaffold composite. Thanks to improved conductivity, they achieved a Coulombic efficiency of 65.7%. However, these solutions require the utilization of expensive materials, and often multi-stages, sophisticated synthesis methods.

Commercially used graphite exhibits relatively low initial irreversible capacity and is a cheaper alternative to CNTs or graphene. Moreover, graphitic electrodes are characterised by high electrical conductivity and decent stability even after hundreds of cycles. Graphite was already successfully applied to enhance the electrochemical

performance of various composite materials [25,26], including SiOC and SiCN-derived ceramics [27–33]. Although pure SiCN samples were electrochemically inactive towards lithium ions (capacities up to 40 mAh g^{-1}), SiCN/C composites revealed an enhanced capacity and significantly improved rate capability. It has been stated that ceramic part of the composite has a protective function, stabilizing the electrochemical response of carbon at high current polarisation, whereas carbon provides electronic conductivity and additional storage sites [27,28]. Saleh and Raj [34] demonstrated SiOC-graphite fibres composite with improved electrochemical performance, attributed to the creation of graphite-SiOC interphase. In our recent work, composites prepared from phenyltriethoxysilane (PhTES) and graphite in different ratios were investigated as anodes for high-power energy storage devices. Addition of graphite, although improving capacity values at high current rates, did not decrease the first cycle irreversible capacity [32].

SiOC/graphite composites based on vinyltriethoxysilane (VTES) as a starting preceramic precursor, which are the focus of this work, exhibit high capacities, stable electrochemical behaviour upon multiple cycling and significantly improved the first cycle Coulombic efficiency with respect not only to pure ceramic, but also to analogous $SiOC_{PhTES}$/graphite composites. These blends are synthesized using a sol-gel method with enhanced gelation and drying procedure by applying an innovative approach of high-power ultrasounds. The sonication process ensures a very uniform distribution of graphite flakes inside the preceramic polymer matrix and increases the temperature of sols accelerating the evaporation of solvents and the gelation process. The electrochemical testing of the final ceramic composites reveals a synergistic effect between the components, resulting in considerably enhanced capacity values in comparison to the

pristine ceramic and pure graphite. The electrochemical features are discussed with respect to the microstructural characteristic of the materials. The impact of the microstructural dissimilarities of VTES and PhTES-based SiOC/graphite composites is pointed out, revealing the influence of a type of functional groups in the preceramic polymer on the electrochemical behaviour of the final ceramic material.

2. Experimental

2.1 Preparation of ceramic composites

High purity vinyltriethoxysilane (>98%) was purchased from Sigma-Aldrich (Germany). Synthesis of polysiloxane/graphite blends was conducted using the sol-gel method, with the procedure described in our previous work [32] but with a different alkoxysilane precursor. First, the preceramic precursor was mixed with ethanol (EtOH/Si = 2) and graphite (Graphite, powder, <20 micron, synthetic, Sigma-Aldrich, Germany). Different amounts of graphite were used, namely 2, 4 or 10 g per 0.072 M of precursor. Then HCl-acidified water (pH = 4.5) was added dropwise (H_2O/OEt = 1) and mixture was boiled for 1.5 h. Next, the obtained sols were cooled down and gelled in polypropylene test tubes. The gelation process was accompanied with homogenization using high-power ultrasounds (UP200St, Hielscher Ultrasound Technology, Germany) by immersing a titanium sonotrode into sol/graphite mixture. The sonication process accelerated evaporation of solvents and caused intense mixing of the sol with graphite. The sonication was stopped when the gel had a tar-like consistency in order to avoid sedimentation and agglomeration of the graphite particles. Then, the gels were dried for 5 days, increasing temperature from 80 to 120°C. Such a treatment leads to the homogenous distribution of the graphitic flakes within the gel, as presented on SEM images and EDS mapping (Figure S1 in Supplementary Information (SI)). To obtain the

final ceramics, the polysiloxane/graphite xerogels were pyrolyzed at 1000°C for 1 h under argon atmosphere. The heating rate was 100°C h^{-1}.

The composites obtained from vinyltriethoxysilane with the respective amount of carbon per 0.072 M of precursor are denoted as $SiOC_{VTES}$/C2g, $SiOC_{VTES}$/C4g, $SiOC_{VTES}$/C10g. For the materials after pyrolysis, for 1 g of a pristine $SiOC_{VTES}$ 0.25 g, 0.5 g and 1.25 g of graphite is added. That corresponds to approx. 20, 33 and 55 wt.% of graphite in the composite samples, respectively. The above estimations are in the agreement with the results of the elemental analysis, Table 1.

2.2 Electrochemical cells preparation

The SiOC/graphite ceramic composites were milled in ball mill (Mixer Mill, MM200, Retsch, Germany) to obtain powder with median particle size of 10 μm. Then the slurry was obtained from 85 wt.% of the ceramic powder (active material), 10 wt.% polyvinylidene fluoride (PVDF, Solef 5130, Solvay, Germany) dissolved in N-methyl-2-pyrrolidone (BASF, Germany) and 5 wt.% Carbon Black Super P® (Imerys Graphite & Carbon, Swizerland) and 1-2 g of NMP to adjust viscosity. The slurry was casted on a copper foil (10 μm, Copper SE-Cu58 Schlenk Metallfolien GmbH& Co. KG, Germany) using doctor blade technique. Obtained layers were then dried at 80°C for 2 days, cut into 10 mm electrodes, weighted and dried under vacuum atmosphere at 80°C for 24 h in Büchi oven. After that electrodes were transported into glove box (MBraun Glove Box Systems) filled with argon.

Swagelok® type two-electrode cells were assembled for electrochemical measurements, with SiOC/graphite composites or pure SiOC as working electrodes, 1 M $LiPF_6$ in ethylene carbonate:dimethyl carbonate (EC:DMC 1:1 v/v, Sigma-Aldrich, Germany) as electrolyte, quartz filter paper (GF-2, 45 μm thick, Macherey-Nagel GmbH

& Co. KG, Germany) as separator, and lithium foil (Sigma Aldrich, Germany) as counter/reference electrode. The active material loading was approx. 2 mg cm^{-2}.

2.3 Electrochemical measurements

Galvanostatic cycling was performed using multichannel battery interface (Atlas 0961, Atlas-Sollich, Poland), and potentiostat-galvanostat SP200 (BioLogic Science Instruments, France). Potential limits were set between 0.005 V and 3 V (*E* vs. Li/Li^+). The current rates and capacities are calculated per mass of active material. The error bars for key samples were determined as standard deviation from three or more separate measurements for each cycle. Cyclic voltammetry (CV) was conducted on potentiostat-galvanostat SP200 (BioLogic Science Instruments, France).

2.4 Material characterization

Elemental analysis was performed using carbon analyzer (Leco C-200, Leco Corporation, USA) and a nitrogen/oxygen analyzer (Leco TC-436, Leco Corporation, USA). The amount of carbon and oxygen was directly measured, and the amount of silicon was calculated as a difference to 100% assuming no other elements are present in the samples and the amount of residual hydrogen is negligible. The errors for carbon and oxygen content were calculated as standard deviation for at least three separate measurements, while error for silicon content was calculated according to the rule of uncertainty propagation. X-ray diffraction measurements was carried out using powder diffractometer Stoe STADI P equipped with Mo anode. Micro-Raman spectra was performed using confocal micro-Raman spectrometer (InVia, Renishaw) with an argon ion laser (514 nm) within the wavenumber range of 100-3200 cm^{-1}. The fitting process of Raman spectra was performed using OriginPro2016 software after background subtraction. The D3 band was fitted using Gaussian curve and the remaining bands were

fitted using Lorentzian peak. XPS analysis was conducted on a VG ESCALAB spectrometer with monochromatic Al Ka source. Magic angle spinning nuclear magnetic resonance (MAS-NMR) measurements were conducted on the Bruker Avance Ultrashield 500 MHz spectrometer. ^{29}Si NMR spectra were recorded with the following parameters: single pulse sequence, ^{29}Si frequency: 139.11 MHz, $\pi/8$ pulse length: 2.5 ms, recycle delay: 100 s, 1k scans, external secondary reference: DSS. 3.2 mm zirconia rotors filled with samples were spun at 8 kHz under air flow. The morphology was characterized by transmission electron microscope TEM (FEI, G2 F20X-Twin 200 kV, FEG). To identify the chemical elements used, energy-dispersive X-ray spectroscopy EDS (EDAX, RTEM model SN9577, 134 eV) spectra were recorded in designated areas and maps of elements. Measurements were made in TEM mode (bright-field) and STEM mode (HAADF and EDX detectors). Preparation of the samples was the following: dispersion of a few milligrams of the sample $SiOC_{VTES}$, $SiOC_{VTES}$/C2g or $SiOC_{VTES}$/C10g in ultrasound in ethanol (99.8% anhydrous) occurred within 5 s, then a drop (5 mL) was applied on carbon-coated copper mesh with holes (Lacey type Cu 400 mesh, Plano) and evaporation of the solvent occurred at room temperature. The SEM imaging was performed on Phenom XL Scanning Electron Microscope (ThermoFisher Scientific, Poland) equipped with energy dispersive X-ray (EDX) microanalyser.

3. Results and discussion

Table 1 shows the results of the elemental analysis of $SiOC_{VTES}$ and its composites with graphite. The amount of free carbon increases and the amount of oxygen and silicon decreases with increasing graphite to silicon ratio. The results of the elemental analysis confirm the tentative estimation of the graphite/ceramic ratio, assuming no reaction between graphitic powder and the preceramic polymer (see experimental section). Thus,

the addition of graphite powder to preceramic sols appears to be an effective way to tailor carbon content in the SiOC composites.

Table 1. Results of elemental analysis of $SiOC_{VTES}$ and $SiOC_{VTES}$/graphite composites.

Material	C	O	Si	C_{free}	Empirical formula
	wt.%				
$SiOC_{VTES}$	27.1±0.1	32.2±1.5	40.7±1.5	21.8	$SiO_{1.39}C_{1.56}$
$SiOC_{VTES}$/C2g	44.4±0.8	26.0±0.4	29.6±0.9	41.5	$SiO_{1.54}C_{3.51}$
$SiOC_{VTES}$/C4g	54.7±0.3	21.6±0.3	23.7±0.4	52.6	$SiO_{1.59}C_{5.39}$
$SiOC_{VTES}$/C10g	74.0±0.2	13.1±0.5	12.9±0.5	73.4	$SiO_{1.78}C_{13.41}$

Microstructural evolution of the ceramic material in the presence of graphite has been evaluated using Raman spectroscopy (Figure 1). The spectra of all investigated samples reveal two characteristic bands: the D-band, at around $1335 \pm 10\ cm^{-1}$, originating from disordered graphene layers and the G band at around $1580 \pm 10\ cm^{-1}$ which corresponds to ideal graphitic lattice [35]. Bands around $2685 \pm 20\ cm^{-1}$ and $2900 \pm 20\ cm^{-1}$ represent overtones of D mode and combination of D+G bands, respectively [35,36]. The addition of graphite diminishes the D/G band intensity ratio, due to the presence of highly ordered graphitic lattice in the composite structure. In order to get more insight into the microstructural features of the investigated samples, the first order spectra were deconvoluted [35–37]. The deconvolution reveals three additional bands of D2, D3 and D4 related to surface graphene layers, amorphous carbon and disordered graphene lattice, respectively [35]. The deconvoluted spectra are shown in Figure 1 b)-f). Moreover, the details such as bands positions, intensity, area, intensity ratio I_{D1}/I_G and I_{D2}/I_G obtained from the fitting of the Raman spectra of the investigated samples are gathered in Table 2 and Tables S1 and S2 (SI).

Table 2. Bands positions, bands intensity and intensity ratios of relevant bands calculated from the deconvoluted Raman spectra.

Material	D4		D1		D3		G		D2		I_{D1}/I_G	I_{D2}/I_G
	cm^{-1}	Intensity	cm^{-1}	Intensity	cm^{-1}	Intensity	cm^{-1}	Intensity	cm^{-1}	Intensity		
$SiOC_{VTES}$	1203	0.038	1329	1.01	1534	0.29	1570	0.26	1603	0.56	3.88	2.15
$SiOC_{VTES}$/C2g	1195	0.052	1328	0.92	1537	0.23	1578	0.60	1607	0.44	1.53	0.73
$SiOC_{VTES}$/C4g	1205	0.077	1339	0.56	1534	0.13	1579	0.74	1613	0.30	0.76	0.41
$SiOC_{VTES}$/C10g	1210	0.030	1348	0.27	1530	0.004	1577	0.91	1610	0.12	0.30	0.13
Graphite	-	-	1348	0.22	-	-	1573	0.97	1611	0.04	0.23	0.04

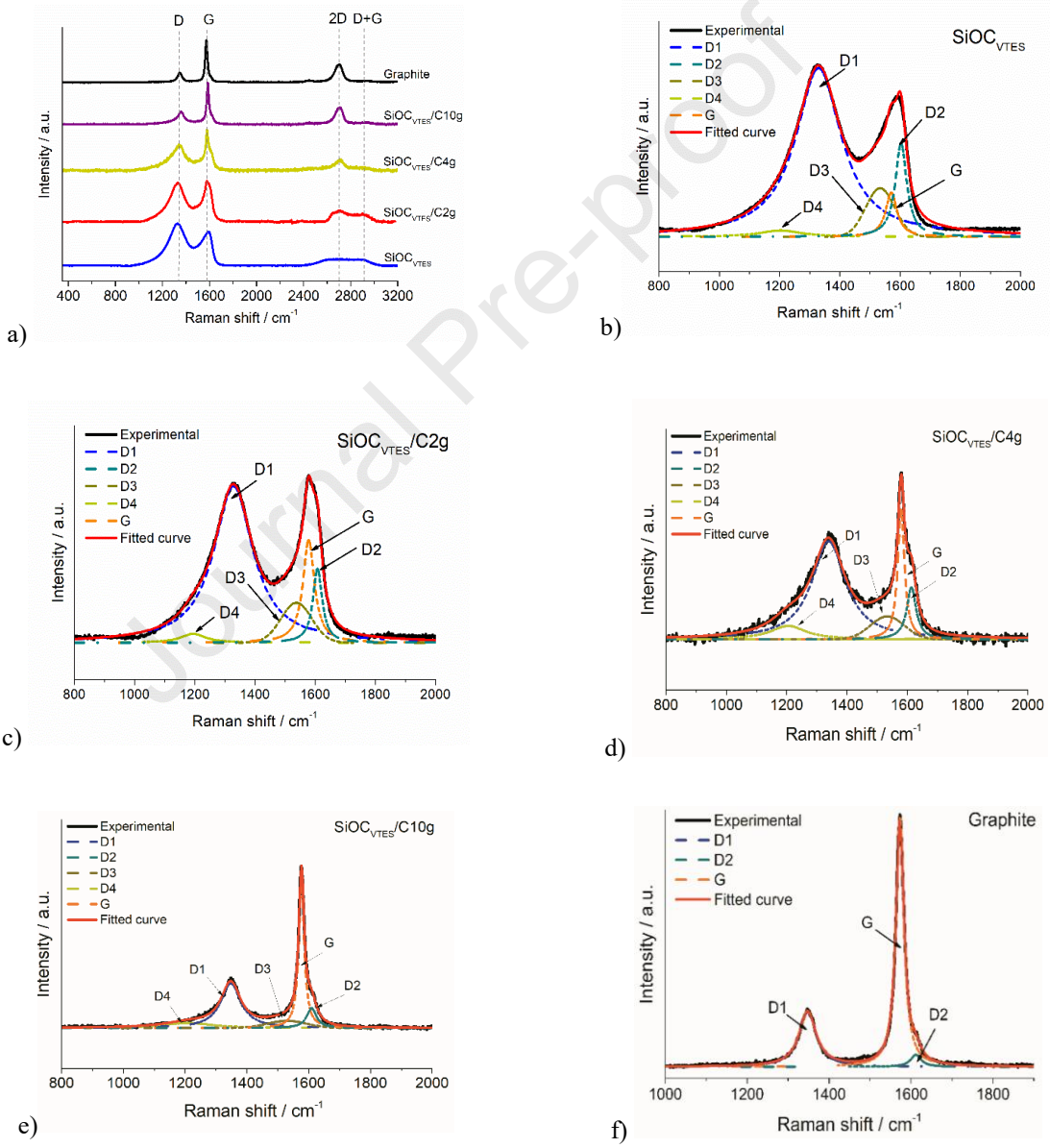

Figure 1. Raman spectra of the a) $SiOC_{VTES}$, $SiOC_{VTES}$/graphite composites and pure graphite (spectra after background subtraction). Deconvoluted Raman spectra of b) $SiOC_{VTES}$, c) $SiOC_{VTES}$/C2g, d) $SiOC_{VTES}$/C4g, e) $SiOC_{VTES}$/C10g, f) graphite samples.

The analysis of the deconvoluted Raman spectra of the SiOC/graphite composites (Table 2, Figure 1 b)-e)) reveals a significant decrease of I_{D1}/I_G (from 3.88 to 0.30) and I_{D2}/I_G (from 2.15 to 0.13) ratios with the increasing amount of graphite in the sample. This originates from the increasing intensity of G band due to the increasing share of ordered graphitic clusters in the carbon phase of the composites.

Figure 2 presents the X-ray diffractograms of the pristine SiOC ceramics, graphite and the composites. Pure graphite shows four sharp reflexes at 12, 19.1, 20.1 and 33.5° (values for 2theta Mo K_α; the corresponding values for Cu K_α are equal to 26.2, 42.2, 44.5 and 77.4°, respectively), that can be ascribed to [002], [100], [101] and [110] Bragg reflexes of typical hexagonal graphite structure, and proves good crystallinity of the material [38,39]. On the other hand, $SiOC_{VTES}$ ceramic exhibits only a broad halo with a centre at around 10° (21.8° for Cu K^α) indicating the presence of amorphous silica [10,40]. The SiOC-graphite composites reveal graphitic reflexes (the same position and shape), with intensity increasing for the higher amount of graphite. Thus, we can conclude the presence of the separate graphitic phase embedded in the amorphous SiOC matrix.

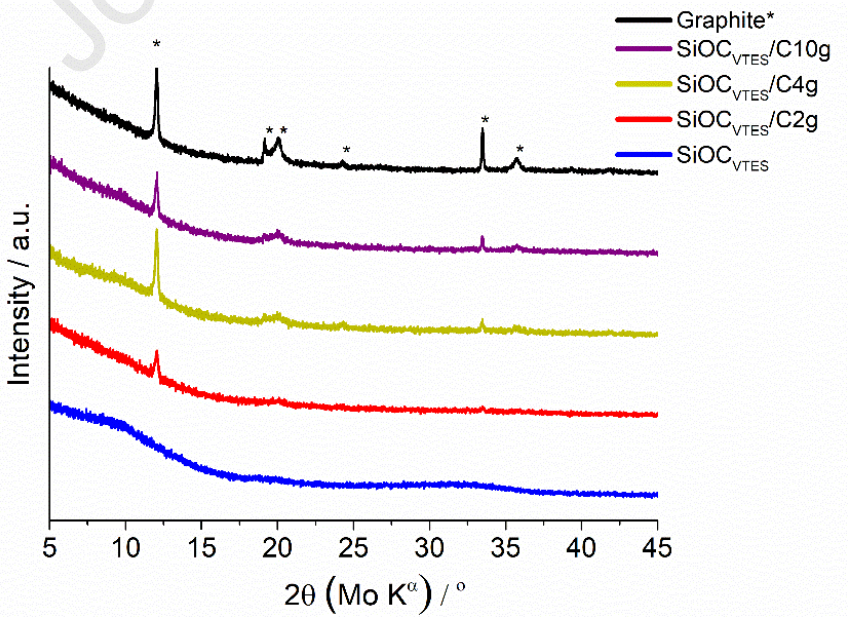

Figure 2. X-ray diffractograms of $SiOC_{VTES}$, $SiOC_{VTES}$/graphite composites and graphite.

^{29}Si MAS NMR spectra of $SiOC_{VTES}$ and its composite with graphite are shown in Figure 3. Addition of graphite to the ceramic phase leads to broadening and a slight shift of the peaks, but there are no significant changes identified in the share of the silicon tetrahedra ($\underline{Si}O_4$, $\underline{Si}O_3C$ and $\underline{Si}O_2C_2$), as presented in Table 3.

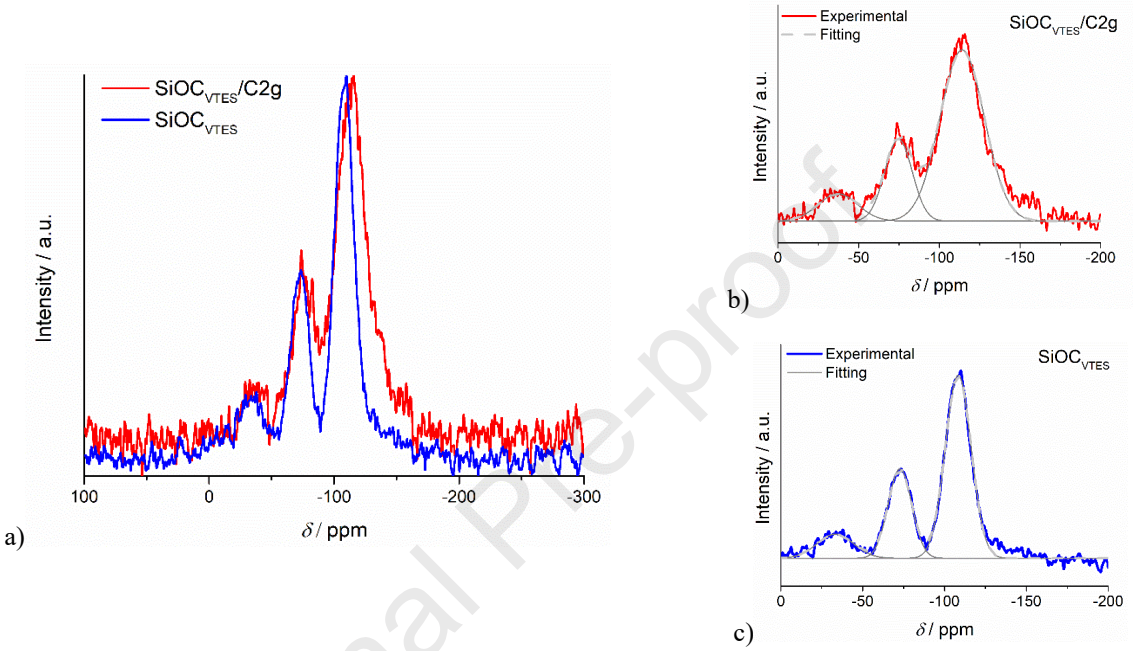

Figure 3. a) Comparison of ^{29}Si MAS NMR spectra of $SiOC_{VTES}$ and $SiOC_{VTES}$/C2g samples; deconvolution of: b) $SiOC_{VTES}$/C2g and c) $SiOC_{VTES}$ spectrum.

Thus, we can state that no reaction between graphite and $SiOC_{VTES}$ during synthesis and pyrolysis occurs. This finding is in agreement with our previous report on $SiOC_{PhTES}$-based composites with graphite [32]. Note that pure silicon oxycarbide prepared from VTES precursor using sol-gel method without ultrasounds [6] exhibits slightly lower carbon content (22.9 wt.% vs 27.1 wt.%) and significantly lower share of mixed bonds silicon tetrahedra (7.8% of $\underline{Si}O_3C$ and lack of $\underline{Si}O_2C_2$ [6] vs 27.2% of $\underline{Si}O_3C$ and 11.4% of $\underline{Si}O_2C_2$) in comparison to $SiOC_{VTES}$ discussed in the present work. This suggests that high power ultrasounds applied during sol-gel synthesis provoke additional reactions involving vinyl group, and, in consequence, changes in the microstructure of the final

ceramics. Moreover, ultrasounds cause fast mixing and temperature rise, which enhance evaporation of solvents, resulting in less solvents molecules trapped in the gel. This, in turn, signifies less oxygen consuming free carbon during the pyrolysis process.

Table 3. Data from the deconvolution of ^{29}Si MAS NMR spectra of $SiOC_{VTES}$ and $SiOC_{VTES}$/C2g samples.

Material	$\underline{Si}O_4$		$\underline{Si}O_3C$		$\underline{Si}O_2C_2$	
	δ / ppm	%	δ / ppm	%	δ / ppm	%
$SiOC_{VTES}$	-108.3	61.3	-72.7	27.2	-33.3	11.4
$SiOC_{VTES}$/C2g	-114.1	69.5	-74.6	23.1	-37.1	9.9

Surface composition and binding energies of the ceramic materials have been studied by XPS measurements (see Figure S2, S3 and Table S3 in SI). The surface composition differs significantly with the bulk composition obtained by the elemental analysis. Nevertheless, for the scope of this study, the XPS analysis provides the comparison of the binding energies between the pure ceramics and the SiOC/graphite composites. The deconvolution of C1s spectra reveals the signal at 284.0-284.4 eV, which may be assigned to two types of bonds: *i)* C=C bonds representing ordered graphitic layers in the investigated materials and *ii)* C-Si bonds corresponding to carbon in mixed silicon tetrahedral [41–43]. Further, the signals at binding energy (BE) of 284.8-285.2 eV correspond to C-C bonds, originating from a disordered free carbon phase within the ceramic materials [44]. The signals of C-O and C=O are identified at higher binding energies [45]. SiOC/graphite composites exhibit noticeably higher band corresponding to C=C bonds, which may be explained by a higher share of ordered graphitic carbon in the sample. Consequently, the peak at approx. 285 eV is lower as the free carbon phase represents a smaller share of the total amount of carbon in the sample. Addition of graphite to the samples decreases the overall amount of silicon in the sample, which causes more noise in the signal of the Si 2p spectrum for $SiOC_{VTES}$/C10g (Figure S3 in

SI). Therefore, it is ambiguous to conclude on the share of mixed bonds silicon tetrahedra based on the XPS Si 2p spectrum of the composite sample.

TEM micrographs show the amorphous structure of pure SiOC (Figure 4 a) and two different microstructures represented by amorphous SiOC and the more ordered carbon material (Figure 4 b, c) in SiOC/graphite composites. Quantitative differences between samples $SiOC_{VTES}$/C2g and $SiOC_{VTES}$/C10g are difficult to identify based on TEM (Figure 4 b, c) and STEM measurements (Figure S4 in SI). Nevertheless, the results of STEM-EDX analysis of the $SiOC_{VTES}$/C10g sample (Figure 4 d) confirm the elemental composition corresponding to the areas of amorphous SiOC, where silicon and oxygen dominate, and the more ordered region containing exclusively carbon. The elemental maps coincide with the corresponding areas of silicon and oxygen for SiOC and carbon for C areas.

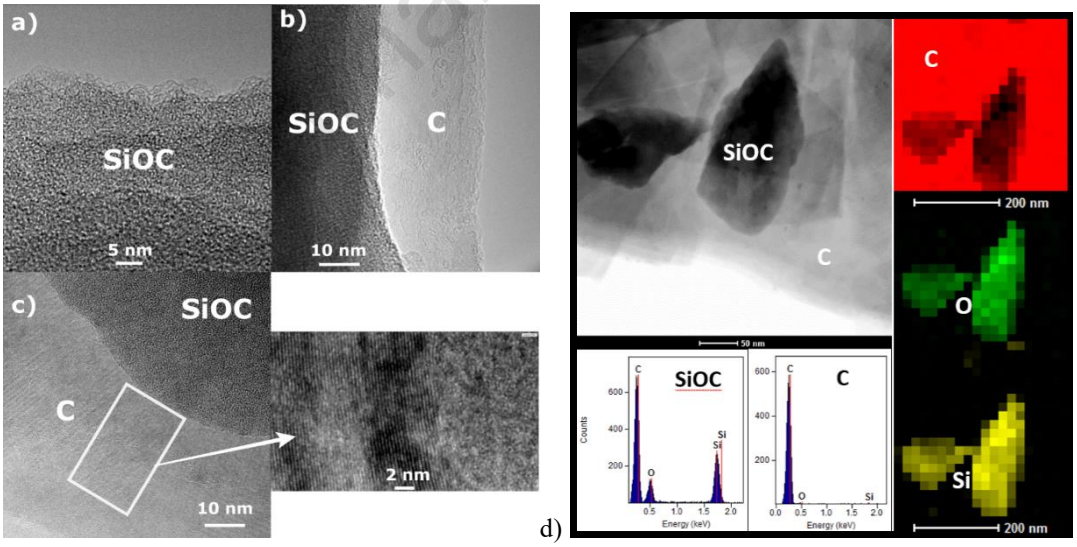

Figure 4. High resolution TEM images of a) $SiOC_{VTES}$, b) $SiOC_{VTES}$/C2g, c) $SiOC_{VTES}$/C10g samples; d) STEM-EDX of $SiOC_{VTES}$/C10g sample.

In order to assess the electrochemical activity of the investigated composites, cyclic voltammetry (CV), galvanostatic charge-discharge and impedance spectroscopy measurement were performed. Figure 5 a) shows the first three cycles of CV obtained for

$SiOC_{VTES}$ ceramic electrodes with the corresponding galvanostatic charge/discharge cycles (insets). The first CV cycle reveals a slight rise of a cathodic current at 0.7 V, attributed to SEI formation and a steep increase of the current at the potentials below 0.4 V. In the anodic direction $SiOC_{VTES}$ electrode shows one broad peak in the potential range of 0.4-0.8 V with one maximum at approx. 0.6 V. The electrochemical features found by CV are confirmed by galvanostatic charge-discharge transients (insets of Figure 5 a). The irreversible plateau at 0.4 V corresponding to the steep increase of cathodic current on CV curve of $SiOC_{VTES}$ sample may be assigned to irreversible lithium storage in the proximity of oxygen in a silica-rich environment.

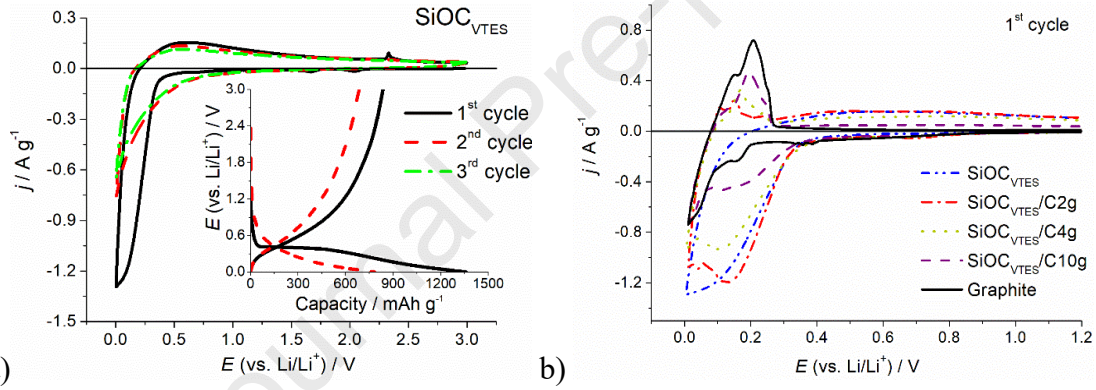

Figure 5. Cyclic voltammetry curves and charge-discharge plots (Insets) recorded for: a) $SiOC_{VTES}$ and b) graphite, $SiOC_{VTES}$ and $SiOC_{VTES}$/graphite composites; sweep rate 0.1 mV s^{-1}, current rate 18.6 mA g^{-1}.

Figure 5 b) depicts the cyclic voltammograms recorded for the investigated SiOC/graphite composites compared with the corresponding pristine ceramics and graphite. The graphite electrode exhibits three characteristic cathodic peaks, at 0.18, 0.13 and 0.09 V vs Li/Li^+, representing three stages of lithium insertion into graphite [46–48], and one small peak at around 0.4 V vs Li/Li^+, related to the formation of solid electrolyte interface (SEI). On the anodic site, two overlapping peaks are observed, attributed to lithium extraction. The peaks are quite broad due to a high scan rate of 0.1 mV s^{-1}.

Note that the increasing amount of graphite in the sample leads to a decrease of

cathodic currents for the first cycle, whereas the peaks attributed to the lithiation of graphite are more pronounced. At the same time, a higher graphite content results in higher anodic currents, compared to SiOC, in the 0-0.25 V potential range with peaks typical for delithiation of graphite. This confirms the experimental findings using NMR, Raman spectroscopy and XRD, that graphite remains unreacted in the composite, while both components are electrochemically active.

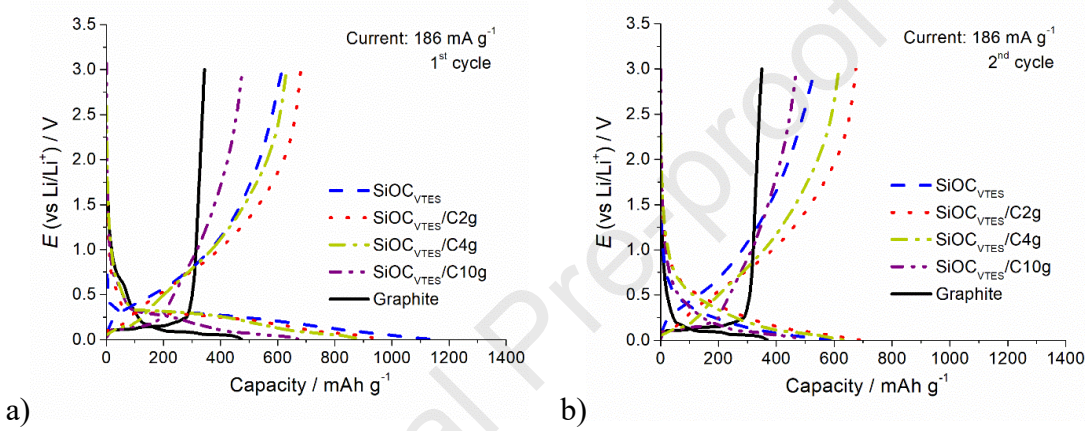

Figure 6. Galvanostatic charge-discharge curves of the a) first and b) second cycle of graphite, $SiOC_{VTES}$ and $SiOC_{VTES}$/graphite composites.

Figure 6 a) and b) show the first and second lithiation-delithiation curves for $SiOC_{VTES}$ and $SiOC_{VTES}$/graphite composites recorded at 186 mA g^{-1}. The observed plateaus correspond well to the peaks observed on CV curves. In the first cycle of $SiOC_{VTES}$ sample, a long, irreversible plateau is found at 0.4 V. In the case of $SiOC_{VTES}$/graphite composites the plateau shortens with the increasing amount of graphite in the sample, resulting in a lower irreversible capacity of the first cycle. The intercalation stages of graphite are observed at approx. 0.09, 0.13 and 0.18 V. It is worth mentioning that the capacity and Coulombic efficiency of the pristine graphitic material is lower than reported in literature [49,50] and by electrode suppliers [51,52]. In the present study, however, the synthetic graphitic flakes (Sigma-Aldrich) have been used,

characterised by higher specific surface area and a lower crystallinity than vein or natural flake graphite [53]. This leads to a more defective structure, and it results in higher first cycle losses and lower reversible capacities as demonstrated and discussed by Gnanaraj *et al.* [54]. Formation of SEI and related capacity losses are significantly affected by crystallographic orientation of edges of graphitic flakes (zigzag and armchair edges of different reactivity), as analysed by Bernardo *et al.* [55]. The first lithiation curve of the investigated graphite exhibits slopping plateau at approx. 0.5 V (Figure 6 a), which is characteristic for the graphite flakes with higher fraction of the zigzag edges compared to the armchair ones. Such morphology promotes co-intercalation of solvent molecules leading to an exfoliation of graphite and an increase of the first cycle irreversible capacity [55]. Nevertheless, in the case of $SiOC_{VTES}$/graphite composites, the presence of graphite lowers the first cycle irreversibility (see Table 4), in contrast to analogous composites based on $SiOC_{PhTES}$ and graphite [32].

Table 4. Average values of reversible C_{rev} and irreversible C_{irrev} capacity of the first cycle upon polarisation with 186 mA g^{-1}, Coulombic efficiency η of the first cycle and the efficiency η' of the reversible capacity after 270 cycles ($C_{rev270th}/C_{rev1st}$). The samples were polarised with different current rates: 186 mA g^{-1}x100, 744 mA g^{-1}x50; 1860 mA g^{-1}x100, 186 mA g^{-1}x20.

Material	1st cycle C_{rev} / mAh g^{-1}	1st cycle C_{irrev} / mAh g^{-1}	270th cycle C_{rev} / mAh g^{-1}	1st cycle C_{rev} recovered below 1.5 V / %	η / %	η' / %
Graphite	312	130	234	90	71	75
$SiOC_{VTES}$	674	549	224	76	55	33
$SiOC_{VTES}$/C2g	730	320	519	76	70	71
$SiOC_{VTES}$/C4g	630	268	464	77	70	73
$SiOC_{VTES}$/C10g	476	195	341	79	71	72

The shapes of charge-discharge transients and cyclic voltammetry curves registered for $SiOC_{VTES}$/graphite composites are somewhat in between pure $SiOC_{VTES}$ and graphite. Similar tendency is found for $SiOC_{PhTES}$/graphite composites [32]. The lithiation potentials of composites decrease in comparison to those of pure SiOC, being of

advantage for commercial applications (lower hysteresis). The presence of graphite component significantly improves the electrochemical performance of $SiOC_{VTES}$. This is rationalized by an increased ionic diffusion and improved electrical conductivity originating from addition of graphite.

Impedance spectroscopy measurements have been performed in order to get insights into electric properties of the composites. Series of Nyquist spectra recorded during first lithiation cycle of $SiOC_{VTES}$/C2g, $SiOC_{VTES}$ and graphite are presented in Figure 7, Figure S5 a) and b) (SI), respectively. At 2 V, where no reaction with Li ions takes place, the spectra consist of semicircle and straight almost vertical line for all three samples. The difference between the spectra of the composite and pure components is in the diameter size of the high-frequency semicircle, which decreases with increasing graphite content. At 1 V second semicircle in the mid-frequency region appears, which may arise from adsorption of electrolyte species on the electrode surface, increasing the resistance. At 0.75 V this semicircle becomes smaller. Such tendency is observed for all three samples. At potentials below 0.35 V, in the mid-frequency region, pure ceramic sample exhibits typical Warburg shaped line, which becomes steeper at low frequencies, whereas graphite sample shows flat semicircle, and Warburg line in low frequencies. The composite sample in the mid- and low-frequency region exhibits a behaviour similar to the graphite electrode, indicating intercalation of lithium in graphitic planes.

High frequency semicircle is attributed to a migration of lithium ions through the surface films on the active material particles, formation of the SEI film and resistance of electronic contacts (current collector, conductive additive, binder) [56–60]. The mid frequency semicircle is related to the resistance of the charge transfer reaction at electrode/electrolyte interphase [57,60]. The Warburg line at low-frequency region

represents solid state diffusion of lithium ions in the particles of active material. When the line becomes steep it represents capacitive behaviour (accumulation of Li^+ in the bulk). It is worth noticing that for $SiOC_{VTES}$/C2g and graphite samples the diameter of both semicircles (high- and mid-frequency), decreases with the progress of the lithiation process (decreasing the potential). This is in contrast with impedance spectra for lithiation of other types of graphite reported in literature [57,58]. Increase of impedance at low potentials for graphite is explained by complicated phenomena at the interphase between graphite and surface film [57]. Also, as explained by Zhang *et al.* [58], the resistance of SEI is influenced by two opposite effects: *i)* formation of conductive surface film, which decreases the resistance, and *ii)* expansion of graphite upon lithiation, which increases the resistance. Therefore, by decreasing the potential one can notice decrease or increase of impedance related to SEI. On the other hand, Gnanaraj *et al.* [54] observed a decrease of high- and mid- frequency semicircles upon lithiation for disordered carbons. The lowering of charge transfer resistance (mid-frequency semicircle) with the potential decrease they attributed to the Butler-Volmer type kinetics, whereas the decrease of the SEI resistance (high-frequency semicircle) they explained by reversible changes in surface film upon lithiation. The tendencies in Nyquist plots upon first cycle lithiation process, observed for the investigated materials, suggests creation of low-resistive SEI and small volume changes upon lithiation for all the three samples. Moreover, addition of graphite to the ceramic lowers the charge transfer resistance and the resistance of the surface film, which supports the hypothesis that graphite increases electric conductivity and creates diffusion paths for lithium, similarly to other forms of carbon as reported in literature [19,20].

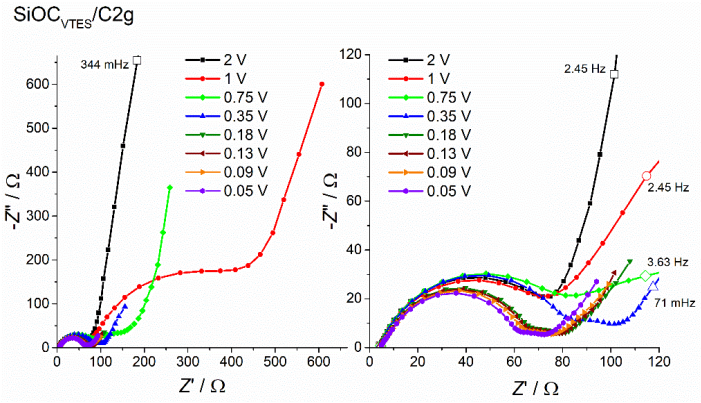

Figure 7. Nyquist plots of SiOC$_{VTES}$/C2g electrode.

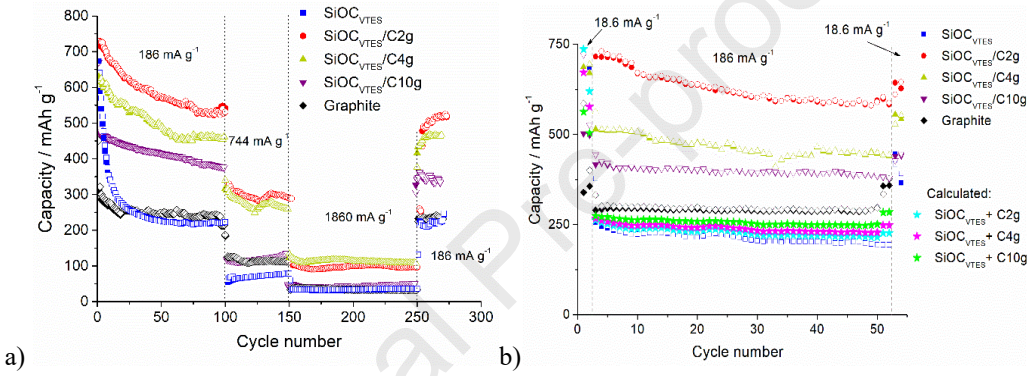

Figure 8. a) Average capacity values as a function of cycle number for graphite, SiOC$_{VTES}$ and SiOC$_{VTES}$/graphite composites recorded at different current rates, b) Comparison of the results obtained for the SiOC$_{VTES}$/graphite composites with the capacities obtained as an arithmetic calculation (depicted as stars) taking into account the ratio of the components in the composites (SiOC$_{VTES}$ + graphite).

To evaluate the electrochemical stability and capacity values of the obtained composites, galvanostatic charge-discharge tests have been conducted. Figure 8 and Figure S6 (SI) show the galvanostatic cycling of the investigated materials with different current rates. Selected values from these measurements are collected in Table 4 and Table S4 (SI).

All SiOC$_{VTES}$/graphite composites exhibit much higher capacities than pure graphite and SiOC$_{VTES}$. The highest capacities are recorded for the smallest graphite to ceramic ratio, namely SiOC$_{VTES}$/C2g. For this composite, the reversible capacity of ~630

mAh g^{-1} is recorded at 18.6 mA g^{-1} after 50 charge discharge-cycles, and ~520 mAh g^{-1} at 186 mA g^{-1} after 270 cycles. The most stable capacities among investigated composite are found for $SiOC_{VTES}$/C10g, with around 400 mAh g^{-1} obtained at 186 mA g^{-1}. The composites with low graphite content reveal the best performance at the highest investigated current rate (1.86 A g^{-1}) ($SiOC_{VTES}$/C2g and $SiOC_{VTES}$/C4g). These composites recover capacities of approx. 100 mAh g^{-1}, while the composite $SiOC_{VTES}$/C10g reaches half of this value (~50 mAh g^{-1}). These results confirm the literature reports that the ceramic part stabilizes the carbon component upon lithiation/delithiation processes [27,61]. However, a certain equilibrium between ceramic and free carbon phase, which is close to 1:1 weight ratio, has to be preserved for a prolonged electrochemical stability of the materials, especially at high current rates [62]. Such ratio is maintained for the samples with lower graphite content (see Table 1.), which explains their better electrochemical performance. The composites exhibit more stable electrochemical behaviour than graphite at high current densities. Moreover, the electrochemical response of the composites is highly reproducible, as illustrated by small standard deviation from the average capacity values (Figure S7, SI), which indicates homogenous distribution of graphitic flakes within the ceramic matrix.

The microstructural investigations reveal two independent phases of $SiOC_{VTES}$ and graphite present in the composites. Thus, one intuitively expects that the capacity of the composite should equal to the arithmetic sum of the capacities of the single components multiplied by the component ratio. Figure 8 b) shows the corresponding "arithmetic" capacities included in the graph (depicted as stars), directly compared to the measured values. The calculated values oscillate between the capacities of graphite and $SiOC_{VTES}$. It signifies that there is a synergistic effect originating from the addition of graphite to

$SiOC_{VTES}$. It can be rationalized in a way that SiOC protects carbon, leading to high stability comparable to pristine graphite, while graphite provides conductive network. However, such synergy has not been found for carbon-rich PhTES-based composites with graphite [32]. On the other hand, Saleh and Raj [34] studied graphite fibres coated with SiOC ceramics. For thin SiOC films they have also identified a synergistic effect leading to higher capacity values, a higher first cycle Coulombic efficiency and lower hysteresis. It was concluded that the observed synergistic effect was due to graphite-SiOC interface, which exhibits high density of mixed bonds silicon tetrahedral [34,63].

TEM micrographs (Figure 4) clearly reveal that graphitic flakes are well dispersed within the ceramic matrix providing electronic conductivity and additional storage capacity to $SiOC_{VTES}$. Note that the first cycle reversible capacity of composites is much higher than that of the pristine SiOC (70% vs 55%). Irreversible capacity originates from *i)* formation of SEI [64,65] and *ii)* irreversible bonding of lithium in the proximity of oxygen within SiOC ceramic [8].

In order to rationalize the "synergistic effect" hypothesis for $SiOC_{VTES}$/graphite composites and to assess the impact of the microstructure of the ceramic on the electrochemical properties of the resulting composite, we synthesized SiOC/graphite composite based on PhTES precursor with a tailored amount of graphite ($SiOC_{PhTES}/C_{Tailored}$) to achieve similar chemical composition as the best electrochemically performing $SiOC_{VTES}$/graphite sample, namely $SiOC_{VTES}$/C2g. Both composites consist of similar amounts of silicon, oxygen and carbon, (see Table S5, SI), and moreover exhibit similar share of mixed bonds silicon tetrahedra as presented in Table S6 (SI). However, PhTES-based composite contains more disordered carbon originating from organic functional group compared to VTES-based sample, which is

indicated by the lower G band and higher I_{D1}/I_G and I_{D2}/I_G ratios (see Figure S8, and Table S7 in SI). Electrochemical performance of the composites is shown in Figure 9 a) and b). $SiOC_{VTES}$/C2g exhibits noticeably higher capacity values than $SiOC_{PhTES}/C_{Tailored}$ as well as higher first cycle efficiency (69.5% compared to 52.3%). Interestingly, the rate capability test shows, that at the highest tested current densities (1488 mA g^{-1}, which is 4C in terms of graphite), both composites exhibit similar capacity values. This can be explained by a better rate capability of disordered carbons compared to graphitic ones, as presented by Chen et al. for graphite and hard carbon anodes [66]. In contrast, the pure ceramic samples based on PhTES and VTES precursors show significantly different electrochemical behaviour [6,13]. Pristine low-carbon $SiOC_{VTES}$, in contrary to carbon-rich $SiOC_{PhTES}$, exhibits low capacity values and poor stability upon cycling. However, blending of small amount of graphite with VTES-based polysiloxane results in an unusual enhancement of the electrochemical activity toward lithium ions storage and in the decrease of the first cycle irreversible capacity of the resulting ceramic composite. Based on these findings, the following can be stated: *i)* the carbon content plays an important role in the formation of electronically conducted paths within the ceramic, *ii)* the microstructure of the free carbon phase and proportion between ordered and disordered carbons are crucial for electrochemical response (a shape of CV and charge-discharge curves, lithiation and delithiation potentials, irreversible capacity values, rate capability performance etc.), and *iii)* microstructure of the ceramic significantly influences the electrochemical performance of the composites.

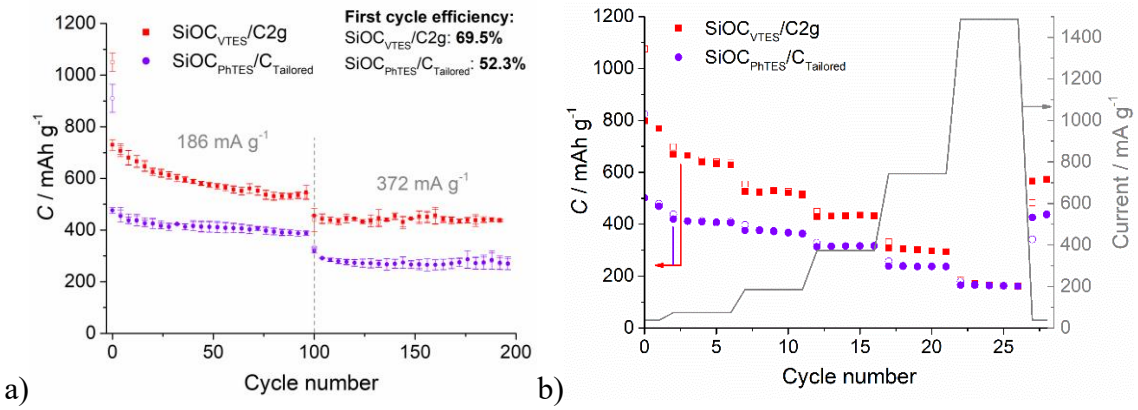

Figure 9. Comparison of electrochemical performance of SiOC/graphite composites having almost identical elemental composition and similar share of mixed bonds silicon tetrahedra, based on VTES and PhTES precursors, a) cycling performance and b) rate capability.

Overall, uniform dispersion of an interconnected conductive carbon network in the SiOC matrix is essential for high performance SiOC anodes. Thus, as demonstrated in our previous works, the in-situ formed free carbon phase from organic functional groups attached to silicon results in much better electrochemical performance of SiOC ceramic in comparison to the ceramic composites obtained by simple mixing carbon and ceramic polymer precursor [27,29,31]. Here, however, the implementation of the high energy ultrasonication leads to highly disordered flakes consisting of several graphene layers, uniformly distributed in the SiOC matrix, as confirmed by TEM micrographics. The enhanced high rate performance of the composites demonstrate that the uniform distribution of carbon promotes electron and ion diffusion in the whole anode. The presence of graphite also leads to much slower capacity fading during initial cycles, with the most stable material containing 74 wt.% of graphite (SiOC$_{VTES}$/C10g). This material shows, however, the lowest capacity among the composites. The composites with lower content of graphite take advantage of: *i)* high reversible capacity of SiOC (630 mAh g^{-1}), *ii)* new storage places provided by graphite and gaps between graphite and ceramic, *iii)* newly available storage sites thanks to improved ionic/electronic conductivity. For SiOC$_{VTES}$/C10g sample, the high graphitic content indeed provides electrochemical

stability, but in parallel, it diminishes the number of the available lithium storage sites coming from the ceramic part.

To examine the morphological changes of the electrodes after cycling, SEM measurements were performed (Figure S9 and S10 (SI)). The electrode layers exhibit some fractures after electrochemical tests. The breaks are more pronounced after prolonged cycling (over 200 cycles) compared to the shorter tests with higher currents (rate capability), especially for the composite based on carbon poor precursor ($SiOC_{VTES}$/C2g) (Figure S10). Moreover, small cracks of the pure ceramic particles ($SiOC_{VTES}$) can be noticed in the high magnification image (Figure S9 b). Carbon-poor ceramic materials are harder and more rigid than carbon-rich ones, hence more susceptible for cracking.

4. Conclusions

This work shows that the addition of graphitic particles to C-poor SiOC ceramic significantly improves the first cycle Columbic efficiency of the ceramic. In order to achieve this improvement, we apply for the first time a simple and cost-efficient method, namely a high power ultrasonication of graphite/preceramic polymer sols leading to highly uniform blends. We show that in this way graphitic layers are effectively split and thus the agglomeration of graphitic flakes does not occur. As a result, a composite contains a well-distributed and interconnected conductive network. The first cycle Coulombic efficiency of the composites equals to 70%, 15% more than that of the pristine $SiOC_{VTES}$. The microstructural studies (^{29}Si MAS NMR, TEM, Raman and XRD) reveal two unreacted phases, graphite and SiOC, present in the composites. A synergistic effect originating from the addition of graphite to $SiOC_{VTES}$ is identified, resulting in much

higher reversible capacities than those calculated arithmetically from the ratio of the components. Comparing the composites based on carbon-poor and carbon-rich precursors, one may conclude that the ratio between ordered and disordered carbon within the ceramic matrix plays an important role for the electrochemical performance.

Acknowledgements

This work was supported by Foundation for Polish Science under REINTEGRATION program, project No POIR.04.04.00-00-4582/17-00. MGZ acknowledges the financial support of a German Research Foundation (DFG) within the project N° GR 4440/4-1.

5. References

[1] N.S. Choi, Z. Chen, S.A. Freunberger, X. Ji, Y.K. Sun, K. Amine, G. Yushin, L.F. Nazar, J. Cho, P.G. Bruce, Challenges facing Lithium Batteries and Electrical Double-Layer Capacitors, Angew. Chemie - Int. Ed. 51 (2012) 9994–10024. https://doi.org/10.1002/anie.201201429.

[2] T.M. Bandhauer, S. Garimella, T.F. Fuller, A Critical Review of Thermal Issues in Lithium-Ion Batteries, J. Electrochem. Soc. 158 (2011) R1–R25. https://doi.org/10.1149/1.3515880.

[3] D. Deng, Li-ion batteries: Basics, progress, and challenges, Energy Sci. Eng. 3 (2015) 385–418. https://doi.org/10.1002/ese3.95.

[4] A.M. Wilson, J.N. Reimers, E.W. Fuller, J.R. Dahn, Lithium insertion in pyrolyzed siloxane polymers, Solid State Ionics. 74 (1994) 249–254. https://doi.org/10.1016/0167-2738(94)90217-8.

[5] H. Sun, K. Zhao, Atomistic Origins of High Capacity and High Structural Stability of Polymer-Derived SiOC Anode Materials, ACS Appl. Mater. Interfaces. 9 (2017) 35001–35009. https://doi.org/10.1021/acsami.7b10906.

[6] M. Wilamowska-Zawlocka, P. Puczkarski, Z. Grabowska, J. Kaspar, M. Graczyk-Zajac, R. Riedel, G.D. Sorarù, Silicon oxycarbide ceramics as anodes for lithium ion batteries: influence of carbon content on lithium storage capacity, RSC Adv. 6 (2016) 104597–104607. https://doi.org/10.1039/C6RA24539K.

[7] M. Halim, G. Liu, R.E.A. Ardhi, C. Hudaya, O. Wijaya, S.H. Lee, A.Y. Kim, J.K. Lee, Pseudocapacitive Characteristics of Low-Carbon Silicon Oxycarbide for

Lithium-Ion Capacitors, ACS Appl. Mater. Interfaces. 9 (2017) 20566–20576. https://doi.org/10.1021/acsami.7b04069.

[8] W. Xing, A.M. Wilson, K. Eguchi, G. Zank, J.R. Dahn, Pyrolyzed Polysiloxanes for Use as Anode Materials in Litium-Ion Batteries, J. Electrochem. Soc. 144 (1997) 2410–2416. https://doi.org/10.1149/1.1837828.

[9] P. Colombo, G. Mera, R. Riedel, G.D. Sorarù, Polymer-derived ceramics: 40 Years of research and innovation in advanced ceramics, J. Am. Ceram. Soc. 93 (2010) 1805–1837. https://doi.org/10.1111/j.1551-2916.2010.03876.x.

[10] G.D. Sorarù, S. Modena, E. Guadagnino, P. Colombo, J. Egan, C. Pantano, Chemical Durability of Silicon Oxycarbide Glasses, J. Am. Ceram. Soc. 85 (2002) 1529–1536. https://doi.org/10.1111/j.1151-2916.2002.tb00308.x.

[11] Y.D. Blum, D.B. MacQueen, H.J. Kleebe, Synthesis and characterization of carbon-enriched silicon oxycarbides, J. Eur. Ceram. Soc. 25 (2005) 143–149. https://doi.org/10.1016/j.jeurceramsoc.2004.07.019.

[12] H. Fukui, H. Ohsuka, T. Hino, K. Kanamura, A Si-O-C composite anode: High capability and proposed mechanism of lithium storage associated with microstructural characteristics, ACS Appl. Mater. Interfaces. 2 (2010) 999–1008. https://doi.org/10.1021/am100030f.

[13] M. Wilamowska, V.S. Pradeep, M. Graczyk-Zajac, R. Riedel, G.D. Sorarù, Tailoring of SiOC composition as a way to better performing anodes for Li-ion batteries, Solid State Ionics. 260 (2014) 94–100. https://doi.org/10.1016/j.ssi.2014.03.021.

[14] H. Konno, T. Morishita, S. Sato, H. Habazaki, M. Inagaki, High-capacity negative electrode materials composed of Si-C-O glass-like compounds and exfoliated graphite for lithium ion battery, Carbon 43 (2005) 1111–1114. https://doi.org/10.1016/j.carbon.2004.12.005.

[15] G. Shao, D.A.H. Hanaor, J. Wang, D. Kober, S. Li, X. Wang, X. Shen, M.F. Bekheet, A. Gurlo, Polymer derived SiOC integrated with graphene aerogel as highly stable Li-ion battery anodes, ACS Appl. Mater. Interfaces. 12 (2020) 46045–46056. https://doi.org/10.1021/acsami.0c12376.

[16] Z. Sang, X. Yan, L. Wen, D. Su, Z. Zhao, Y. Liu, H. Ji, J. Liang, S.X. Dou, A graphene-modified flexible SiOC ceramic cloth for high-performance lithium storage, Energy Storage Mater. 25 (2020) 876–884. https://doi.org/10.1016/j.ensm.2019.11.014.

[17] S.P. Kuksenko, Highly Disordered Silicon-containing Carbon from Polymethylphenylsiloxane as Anode Material for Lithium-Ion Batteries : Anomalous Behavior in Thin Layer, Russ. J. Appl. Chem. 89 (2016) 1237–1244. https://doi.org/10.1134/S1070427216080048.

[18] M.S. Tahir, M. Weinberger, P. Balasubramanian, T. Diemant, R.J. Behm, M. Linden, M. Wohlfahrt-Mehrens, Silicon carboxylate derived silicon oxycarbides

as anodes for lithium ion batteries, J. Mater. Chem. A. 5 (2017) 10190–10199. https://doi.org/10.1039/c7ta01843f.

[19] R. Bhandavat, G. Singh, Stable and efficient li-ion battery anodes prepared from polymer-derived silicon oxycarbide-carbon nanotube shell/core composites, J. Phys. Chem. C. 117 (2013) 11899–11905. https://doi.org/10.1021/jp310733b.

[20] Z. Sang, Z. Zhao, D. Su, P. Miao, F. Zhang, H. Ji, X. Yan, SiOC nanolayer wrapped 3D interconnected graphene sponge as a high-performance anode for lithium ion batteries, J. Mater. Chem. A. 6 (2018) 9064–9073. https://doi.org/10.1039/c8ta01570h.

[21] Y. Li, Y. Hu, Y. Lu, S. Zhang, G. Xu, K. Fu, S. Li, C. Chen, L. Zhou, X. Xia, X. Zhang, One-dimensional SiOC/C composite nanofibers as binder-free anodes for lithium-ion batteries, J. Power Sources. 254 (2014) 33–38. https://doi.org/10.1016/j.jpowsour.2013.12.044.

[22] Z. Liu, D. Guan, Q. Yu, L. Xu, Z. Zhuang, T. Zhu, D. Zhao, L. Zhou, L. Mai, Monodisperse and homogeneous SiOx/C microspheres: A promising high-capacity and durable anode material for lithium-ion batteries, Energy Storage Mater. 13 (2018) 112–118. https://doi.org/10.1016/j.ensm.2018.01.004.

[23] M. Ma, H. Wang, X. Li, K. Peng, L. Xiong, X. Du, Free-standing SiOC/nitrogen-doped carbon fibers with highly capacitive Li storage, J. Eur. Ceram. Soc. 40 (2020) 5238–5246. https://doi.org/10.1016/j.jeurceramsoc.2020.06.034.

[24] L. David, R. Bhandavat, U. Barrera, G. Singh, Silicon oxycarbide glass-graphene composite paper electrode for long-cycle lithium-ion batteries, Nat. Commun. 7 (2016) 10998. https://doi.org/10.1038/ncomms10998.

[25] M.K. Cho, S.J. You, J.G. Woo, J.C. An, S. Kang, H.W. Lee, J.H. Kim, C.M. Yang, Y.J. Kim, Anomalous Si-based composite anode design by densification and coating strategies for practical applications in Li-ion batteries, Compos. Part B Eng. 215 (2021) 108799. https://doi.org/10.1016/j.compositesb.2021.108799.

[26] Y. Cao, T.D. Hatchard, R.A. Dunlap, M.N. Obrovac, Mechanofusion-derived Si-alloy/graphite composite electrode materials for Li-ion batteries, J. Mater. Chem. A. 7 (2019) 8335–8343. https://doi.org/10.1039/c9ta00132h.

[27] M. Graczyk-Zajac, C. Fasel, R. Riedel, Polymer-derived-SiCN ceramic/graphite composite as anode material with enhanced rate capability for lithium ion batteries, J. Power Sources. 196 (2011) 6412–6418. https://doi.org/10.1016/j.jpowsour.2011.03.076.

[28] R. Kolb, C. Fasel, V. Liebau-Kunzmann, R. Riedel, SiCN/C-ceramic composite as anode material for lithium ion batteries, J. Eur. Ceram. Soc. 26 (2006) 3903–3908. https://doi.org/10.1016/j.jeurceramsoc.2006.01.009.

[29] M. Graczyk-Zajac, M. Wimmer, C. Neumann, R. Riedel, Lithium intercalation into SiCN/disordered carbon composite. Part 1: influence of initial carbon porosity on cycling performance/capacity, J. Solid State Electrochem. 19 (2015) 2763–2769.

https://doi.org/10.1007/s10008-015-2814-y.

[30] M. Graczyk-Zajac, M. Wimmer, Y. Xu, G. Buntkowsky, C. Neumann, R. Riedel, Lithium intercalation into disordered carbon/SiCN composite. Part 2: Raman spectroscopy and 7Li MAS NMR investigation of lithium storage sites, J. Solid State Electrochem. 21 (2017) 47–55. https://doi.org/10.1007/s10008-016-3337-x.

[31] M. Wilamowska, M. Graczyk-Zajac, R. Riedel, Composite materials based on polymer-derived SiCN ceramic and disordered hard carbons as anodes for lithium-ion batteries, J. Power Sources. 244 (2013) 80–86. https://doi.org/10.1016/j.jpowsour.2013.03.137.

[32] D. Knozowski, M. Graczyk-Zajac, G. Trykowski, M. Wilamowska-Zawłocka, Silicon oxycarbide-graphite electrodes for high-power energy storage devices, Materials 13 (2020) 1–17. https://doi.org/10.3390/ma13194302.

[33] Z. Wu, X. Cheng, D. Tian, T. Gao, W. He, C. Yang, SiOC nanolayers directly-embedded in graphite as stable anode for high-rate lithium ion batteries, Chem. Eng. J. 375 (2019) 121997. https://doi.org/10.1016/j.cej.2019.121997.

[34] I. Saleh, R. Raj, Three-dimensional architecture of lithium-anodes made from graphite fibers coated with thin-films of silicon oxycarbide: Design, performance and manufacturability, J. Power Sources. 310 (2016) 18–25. https://doi.org/10.1016/j.jpowsour.2016.01.104.

[35] A. Sadezky, H. Muckenhuber, H. Grothe, R. Niessner, U. Pöschl, Raman microspectroscopy of soot and related carbonaceous materials: Spectral analysis and structural information, Carbon 43 (2005) 1731–1742. https://doi.org/10.1016/j.carbon.2005.02.018.

[36] A.C. Ferrari, J. Robertson, Interpretation of Raman spectra of disordered and amorphous carbon, Phys. Rev. B. 61 (2010) 14095–14107. https://doi.org/10.1136/ip.2010.029215.730.

[37] N.P. Ivleva, A. Messerer, X. Yang, R. Niessner, U. Pöschl, Raman Microspectroscopic Analysis of Changes in the Chemical Structure and Reactivity of Soot in a Diesel Exhaust Aftertreatment Model System, Environ. Sci. Technol. 41 (2007) 3702–3707. https://doi.org/10.1021/es0612448.

[38] N.L. Wu, J. Phillips, XRD evidence of preferental orientation of platinium crystallites on graphite, Surf. Sci. 184 (1987) 463–482. https://doi.org/10.1016/S0039-6028(87)80370-9.

[39] Y.J. Liou, W.J. Huang, High Temperature Phase Transitions of Graphene Oxide Paper from Graphite Oxide Solution, J. Mater. Sci. Technol. 30 (2014) 1088–1091. https://doi.org/10.1016/j.jmst.2014.08.006.

[40] J. Li, K. Lu, T. Lin, F. Shen, Preparation of Micro-/Mesoporous SiOC Bulk Ceramics, J. Am. Ceram. Soc. 98 (2015) 1753–1761. https://doi.org/10.1111/jace.13541.

[41] M.Y. Bashouti, Y. Paska, R. Puniredd, T. Stelzner, Silicon nanowires terminated with methyl functionalities exhibit stronger Si – C bonds than equivalent 2D surfaces, Phys. Chem. Chem. Phys. 11 (2009) 3845–3848. https://doi.org/10.1039/b820559k.

[42] R.I.R. Blyth, H. Buqa, F.P. Netzer, M.G. Ramsey, J.O. Besenhard, XPS studies of graphite electrode materials for lithium ion batteries, Appl. Surf. Sci. 167 (2000) 99–106. https://doi.org/10.1016/S0169-4332(00)00525-0.

[43] R.T. Anderson, X. Zang, R. Fernando, M.J. Dzara, C. Ngo, M. Sharps, R. Pinals, S. Pylypenko, M.T. Lusk, A. Sellinger, Direct Conversion of Hydride- to Siloxane-Terminated Silicon Quantum Dots, J. Phys. Chem. C. 120 (2016) 25822–25831. https://doi.org/10.1021/acs.jpcc.6b07930.

[44] M.A. Abass, A.A. Syed, C. Gervais, G. Singh, Synthesis and electrochemical performance of a polymer-derived silicon oxycarbide/boron nitride nanotube composite, RSC Adv. 7 (2017) 21576–21584. https://doi.org/10.1039/c7ra01545c.

[45] G.M. Renlund, S. Prochazka, R.H. Doremus, Silicon oxycarbide glasses: Part II. Structure and properties, J. Mater. Res. 6 (1991) 2723–2734. https://doi.org/10.1557/JMR.1991.2723.

[46] M.D. Levi, D. Aurbach, The mechanism of lithium intercalation in graphite film electrodes in aprotic media. Part 1. High resolution slow scan rate cyclic voltammetric studies and modeling, J. Electroanal. Chem. 421 (1997) 79–88. https://doi.org/10.1016/S0022-0728(96)04832-2.

[47] E.W. Fuller, Y. Liu, J.R. Dahn, S. Tseng, U. von Sacken, Lithium Insertion in High Capacity Carbonaceous Materials, J. Electrochem. Soc. 142 (1995) 2581–2590. https://doi.org/10.1149/1.2050057.

[48] F. Dinkelacker, P. Marzak, J. Yun, Y. Liang, A.S. Bandarenka, Multistage Mechanism of Lithium Intercalation into Graphite Anodes in the Presence of the Solid Electrolyte Interface, ACS Appl. Mater. Interfaces. 10 (2018) 14063–14069. https://doi.org/10.1021/acsami.7b18738.

[49] C. Mao, M. Wood, L. David, S.J. An, Y. Sheng, Z. Du, H.M. Meyer, R.E. Ruther, D.L. Wood, Selecting the Best Graphite for Long-Life, High-Energy Li-Ion Batteries, J. Electrochem. Soc. 165 (2018) A1837–A1845. https://doi.org/10.1149/2.1111809jes.

[50] L.Z. Bai, D.L. Zhao, T.M. Zhang, W.G. Xie, J.M. Zhang, Z.M. Shen, A comparative study of electrochemical performance of graphene sheets, expanded graphite and natural graphite as anode materials for lithium-ion batteries, Electrochim. Acta. 107 (2013) 555–561. https://doi.org/10.1016/j.electacta.2013.06.032.

[51] Pyrotek Inc. product information, https://www.pyrotek.com/primary-solutions/battery-materials; 2021 (accessed August 2021).

[52] MSE Supplies product information,

https://www.msesupplies.com/products/natural-graphite-powder-lithium-ion-battery-anode-a?variant=7138017860; 2021 (accessed August 2021).

[53] M. Simón, A. Benítez, A. Caballero, J. Morales, O. Vargas, Untreated natural graphite as a graphene source for high-performance Li-Ion batteries, Batteries. 4 (2018) 1–9. https://doi.org/10.3390/batteries4010013.

[54] J.S. Gnanaraj, M.D. Levi, E. Levi, G. Salitra, D. Aurbach, J.E. Fischer, A. Claye, Comparison Between the Electrochemical Behavior of Disordered Carbons and Graphite Electrodes in Connection with Their Structure, J. Electrochem. Soc. 148 (2001) A525. https://doi.org/10.1149/1.1368096.

[55] P. Bernardo, J.M. Le Meins, L. Vidal, J. Dentzer, R. Gadiou, W. Märkle, P. Novák, M.E. Spahr, C. Vix-Guterl, Influence of graphite edge crystallographic orientation on the first lithium intercalation in Li-ion battery, Carbon 91 (2015) 458–467. https://doi.org/10.1016/j.carbon.2015.05.001.

[56] R.N. Putra, M. Halim, G. Ali, S.F. Shaikh, A.M. Al-Enizi, T. Fazal, F. Jan Iftikhar, A.N.S. Saqib, High-rate sodium insertion/extraction into silicon oxycarbide-reduced graphene oxide, New J. Chem. 44 (2020) 14035–14040. https://doi.org/10.1039/d0nj02993a.

[57] B. Markovsky, M.D. Levi, D. Aurbach, The basic electroanalytical behavior of practical graphite-lithium intercalation electrodes, Electrochim. Acta. 43 (1998) 2287–2304. https://doi.org/10.1016/S0013-4686(97)10172-4.

[58] S.S. Zhang, K. Xu, T.R. Jow, EIS study on the formation of solid electrolyte interface in Li-ion battery, Electrochim. Acta. 51 (2006) 1636–1640. https://doi.org/10.1016/j.electacta.2005.02.137.

[59] J. Kaspar, M. Graczyk-Zajac, R. Riedel, Determination of the chemical diffusion coefficient of Li-ions in carbon-rich silicon oxycarbide anodes by electro-analytical methods, Electrochim. Acta. 115 (2014) 665–670. https://doi.org/10.1016/j.electacta.2013.10.184.

[60] A. Funabiki, M. Inaba, Z. Ogumi, S. Yuasa, J. Otsuji, A. Tasaka, Impedance Study on the Electrochemical Lithium Intercalation into Natural Graphite Powder, J. Electrochem. Soc. 145 (1998) 172–178. https://doi.org/10.1149/1.1838231.

[61] G. Liu, J. Kaspar, L.M. Reinold, M. Graczyk-Zajac, R. Riedel, Electrochemical performance of DVB-modified SiOC and SiCN polymer-derived negative electrodes for lithium-ion batteries, Electrochim. Acta. 106 (2013) 101–108. https://doi.org/10.1016/j.electacta.2013.05.064.

[62] M. Graczyk-Zajac, L.M. Reinold, J. Kaspar, P.V.W. Sasikumar, G.D. Soraru, R. Riedel, New insights into understanding irreversible and reversible lithium storage within SIOC and SICN ceramics, Nanomaterials. 5 (2015) 233–245. https://doi.org/10.3390/nano5010233.

[63] L. Yu, R. Raj, On the thermodynamically stable amorphous phase of polymer-derived silicon oxycarbide, Sci. Rep. 5 (2015) 1–13.

https://doi.org/10.1038/srep14550.

[64] Y. Matsumura, S. Wang, J. Mondori, Mechanism Leading to Irreversible Capacity Loss in Li Ion Rechargeable Batteries, J. Electrochem. Soc. 142 (1995) 2914–2918. https://doi.org/10.1149/1.2048665.

[65] D. Aurbach, E. Zinigrad, Y. Cohen, H. Teller, A short review of failure mechanisms of lithium metal and lithiated graphite anodes in liquid electrolyte solutions, Solid State Ionics. 148 (2002) 405–416. https://doi.org/10.1016/S0167-2738(02)00080-2.

[66] K.H. Chen, V. Goel, M.J. Namkoong, M. Wied, S. Müller, V. Wood, J. Sakamoto, K. Thornton, N.P. Dasgupta, Enabling 6C Fast Charging of Li-Ion Batteries with Graphite/Hard Carbon Hybrid Anodes, Adv. Energy Mater. 11 (2021) 1–12. https://doi.org/10.1002/aenm.202003336.

Highlights

- SiOC/C composites are prepared by a novel high-power ultrasounds-assisted synthesis
- Graphitic flakes are uniformly distributed and partially exfoliated within the ceramic
- Microstructural dissimilarities of SiOC/C based on various precursors are discussed
- Synergistic effect on electrochemical properties of SiOC/C depends on microstructure
- SiOC/C electrodes exhibit improved first cycle Coulombic efficiency and high capacity